

# Technical Memo

# 892

## **Validation of IFS+RTTOV/MFASIS solar reflectances against GOES-16 ABI observations**

Philippe Lopez, Marco Matricardi and Mark Fielding  
(Research Department)

March 2022

Series: ECMWF technical memoranda

A full list of ECMWF Publications can be found on our web site under:

<http://www.ecmwf.int/en/publications/>

Contact: [library@ecmwf.int](mailto:library@ecmwf.int)

© Copyright 2022

European Centre for Medium Range Weather Forecasts, Shinfield Park, Reading, RG2 9AX, UK

Literary and scientific copyrights belong to ECMWF and are reserved in all countries. This publication is not to be reprinted or translated in whole or in part without the written permission of the Director-General. Appropriate non-commercial use will normally be granted under the condition that reference is made to ECMWF.

The information within this publication is given in good faith and considered to be true, but ECMWF accepts no liability for error, omission and for loss or damage arising from its use.

## Abstract

Solar reflectances simulated by running RTTOV/MFASIS (fast visible simulator) on input meteorological data from ECMWF's operational IFS short-range forecasts are compared with corresponding GOES-16 ABI reflectances observed in channels 0.47, 0.64 and 0.86  $\mu\text{m}$ . This is the first systematic validation of the IFS at wavelengths in the solar spectrum, which is expected to provide additional information about the prediction of meteorological features that are usually not well detected at infrared frequencies (e.g., low-level clouds). Month-long statistics of reflectances as well as individual images are used to identify deficiencies in both the IFS and in the RTTOV/MFASIS radiative transfer model. In the IFS, issues are found in the representation of trade-wind low-level clouds over ocean, shallow convection over the Amazon region and low-level clouds inside the eye of tropical cyclones. On the other hand, this study also confirms the existence of biases resulting from some of RTTOV/MFASIS's simplifications, such as those made in the Rayleigh scattering computations and in the use of a look-up table. These conclusions are confirmed through an independent comparison of IFS with CERES observations. Results from this work are relevant to the developments towards the assimilation of solar reflectances in ECMWF's 4-Dimensional Variational data assimilation system (4D-Var).

## 1 Introduction

Among the wide range of frequencies used by satellite instruments to observe Earth's atmosphere, short-wave (solar spectrum) frequencies have been largely underused in Numerical Weather Prediction (NWP) applications so far, compared with longwave (infrared) and microwave wavelengths. This can be partly justified by the fact that shortwave reflectances exhibit complex sensitivities to clouds, aerosols and surface characteristics, which can be highly heterogeneous. Another reason could be that shortwave measurements do not allow the sampling of the full diurnal cycle. However, observations at visible wavelengths can provide valuable information about clouds (esp. low-level clouds) and aerosols, that is not available from infrared and microwave data. Accurate radiative transfer models exist for the simulation of visible and near-infrared observations in scattering conditions, such as the Discrete-Ordinate-Method (DOM; [Stamnes \*et al.\*, 1988](#)) radiative transfer model. However, the main drawback of these complex simulators for operational NWP applications, especially satellite data assimilation, is their prohibitive computational requirements (running time and memory). Fortunately, faster (but potentially slightly less accurate) simulators using either look-up tables or a limited number of streams have also recently been developed, such as the Method for FAsT Satellite Image Synthesis (MFASIS; [Scheck \*et al.\*, 2016](#)) and the Forward-Lobe Two-Stream Radiance Model (FLOTSAM; under development by R. Hogan at ECMWF; [Escribano \*et al.\*, 2019](#)), respectively.

The recent implementation of MFASIS in RTTOV (Radiative Transfer for TOVS; [Saunders \*et al.\*, 2018](#)) has made it possible to simulate solar reflectances in individual channels of specific satellites. Geostationary satellites are of particular interest because of their wide field of view (FOV), which encompasses extremely varied meteorological situations in a single snapshot. For this reason, a statistical validation of solar reflectances simulated from ECMWF's operational forecast data against GOES-16 ABI observations is performed over two 1-month-long periods. The main purpose is to identify possible deficiencies in both the IFS forecast model and in the RTTOV/MFASIS reflectance simulator. Besides its potential usefulness for improving the forecast model itself (physical parametrizations), this study can also provide guidance in the work towards the assimilation of visible reflectances at ECMWF, especially with regard to the expected quality of the observation operator and the screening of observations.

The observations, the IFS model data and the RTTOV/MFASIS solar reflectance simulator used in this study are introduced in section 2. This section also briefly describes the method to create natural colour

composite images that are employed to investigate specific weather situations. The results of the validation of simulated against GOES-16 ABI reflectances are then presented in section 3. After a short depiction of the background meteorology of the selected two periods, this section provides a detailed general statistical analysis, followed by a study of specific aspects and weather regimes, such as sunglint, trade-wind low-level clouds, Amazonian convection and tropical cyclones. Finally, an independent validation of mean IFS net broadband shortwave fluxes at the top of the atmosphere against CERES observations is briefly presented, to support the conclusions from this study. Summary and conclusions are given in section 4.

## 2 Data and methodology

### 2.1 GOES ABI observations

The observations used in this study are radiances measured by the ABI (Advanced Baseline Imager) on board NOAA<sup>1</sup>'s geostationary satellite GOES-16 in channels 1, 2 and 3 (two visible, one near-infrared). In addition to these three channels, brightness temperatures in channel 14 (longwave window) are employed to provide ancillary information in the validation of IFS simulations. The main characteristics of each channel are summarized in Table 1 and more details can be found in Schmit *et al.* (2005) and Schmit *et al.* (2017). The GOES-16 ABI FOV is centered at 75°W, therefore overlooking the Ameri-

Channel number	Central wavelength [ $\mu\text{m}$ ]	Best resolution [km]	Name	Sensitive to
1	0.47	1	Blue	Clouds and aerosols
2	0.64	0.5	Red	Clouds, fog, ground snow/ice
3	0.86	1	"Veggie"	Clouds and vegetation
14	11.20	2	Longwave window	Cloud top and surface temperature

Table 1: Characteristics of the three GOES ABI channels used in this study. Channel 14 was only used as an ancillary data source for cloud type identification.

cas and surrounding oceans. Full-disk GOES ABI netCDF Level-1b radiance data have been obtained through NOAA's CLASS<sup>2</sup>.

Prior to statistical computations, for a given wavelength  $\lambda$ , observed radiances ( $L_\lambda$ ; in  $\text{W m}^{-2} \text{sr}^{-1} \mu\text{m}^{-1}$ ) are converted to reflectances ( $R_\lambda$ ; unitless) using

$$R_\lambda = \frac{\kappa L_\lambda}{\cos(\theta_{sun})} \quad (1)$$

where  $\theta_{sun}$  denotes the solar zenith angle.  $\kappa$  is given by

$$\kappa = \frac{\pi d^2}{E_{sun}} \quad (2)$$

where  $d$  is the Earth-Sun distance (in Astronomical Units) and  $E_{sun}$  denotes the solar irradiance in the bandpass (in  $\text{W m}^{-2} \mu\text{m}^{-1}$ ). In practice, values of  $\kappa$  are available in each GOES ABI data file for a given channel.

<sup>1</sup>National Oceanic and Atmospheric Administration (USA)

<sup>2</sup>Comprehensive Large Array-data Stewardship System

Finally, observed reflectances are spatially averaged to match the output grid of the IFS+RTTOV/MFASIS simulator (IRM, hereafter; see section 2.3).

## 2.2 IFS model data

The validation proposed in this study focuses on short-range forecasts obtained with ECMWF’s operational IFS (Integrated Forecasting System; Courtier *et al.*, 1994) at a resolution of 9 km and initialized at 0000 UTC. To cover various weather regimes, the validation is performed over two periods: 15 January-15 February 2021 and 15 August-15 September 2021. For both periods, the forecast data are based on version 47R1 of the IFS (documentation available at <https://www.ecmwf.int/en/publications/ifs-documentation>), which was operational between 30 June 2020 and 12 October 2021. Forecast ranges of 15, 17, 19 and 21 hours have been considered so as to sample the diurnal evolution of solar reflectances and to cover a wide range of local viewing angles and sun incidence angles. However, for the sake of brevity, this report focuses on the time of 1700 UTC (i.e. local noon at sub-satellite point). It should be noted that short forecast ranges are selected here in order to match the typical length of background forecasts used in 4D-Var data assimilation at ECMWF. For obvious reasons, the validation is limited to daytime data.

## 2.3 RTTOV/MFASIS reflectance simulator

The simulation of reflectances from IFS forecast data relies on the lookup-table-based radiative transfer model MFASIS (Method for FAst Satellite Image Synthesis) developed by Scheck *et al.* (2016). The recent implementation of MFASIS in RTTOV (Radiative Transfer for TOVS; Saunders *et al.*, 2018) allows the simulation of reflectances from IFS input data, in the way they would be measured in a set of specific channels by a given spaceborne instrument, such as GOES-16 ABI. In particular, the actual response function of individual channel as sampled by the instrument is taken into account in the radiative transfer computations. Results from this study have been obtained using RTTOV version 12.2.

### 2.3.1 Inputs

The required input IFS data are three-dimensional model-level fields of temperature, specific humidity, cloud fraction, cloud liquid water, cloud ice and snow content; plus the following two-dimensional fields (mostly surface): land-sea mask, logarithm of surface pressure, sea ice cover, snow depth, snow density, skin temperature, 10-metre meridional and zonal wind components, 2-metre dry-bulb and dew-point temperatures, and convective available potential energy (CAPE).

### 2.3.2 Special features

Since ECMWF’s version of RTTOV/MFASIS does not include a dedicated specification of reflectances over snow-covered land, a simple parametrization was introduced, which assumes that the reflectance  $R_{\lambda}^{snow}$ , depends on the skin temperature  $T_{skin}$  [K] and on the high-vegetation fractional cover  $f_{hveg}$  [0-1], as

$$R_{\lambda}^{snow} = \max \left\{ R_{max}^{snow} - \left[ \max \left( \frac{T_{skin} - 268.15}{12}, 0 \right) \right]^2, R_{min}^{snow} \right\} \quad (3)$$

where  $R_{max}^{snow} = 0.85 - 0.45 f_{hveg}$  and  $R_{min}^{snow} = 0.50 - 0.25 f_{hveg}$ . This formulation accounts for the observed non-linear decrease of surface snow albedo with increasing temperature (e.g., Roesch *et al.*, 1999). It

also includes the observed reduction of snow-pack reflectance in regions with high vegetation (e.g., [Betts and Ball, 1997](#)). The overall reflectance  $R_\lambda$  of a given snow-affected land point is then computed as

$$R_\lambda = R_\lambda^{land} + (R_\lambda^{snow} - R_\lambda^{land}) \times f_{snow} \quad (4)$$

where  $R_\lambda^{land}$  and  $f_{snow}$  denote the reflectance of snow-free land (currently set to 0.25) and the snow fractional cover, respectively. The latter is estimated as  $f_{snow} = \min(10000 \frac{h_{snow}}{\rho_{snow}}, 1)$ , where  $h_{snow}$  and  $\rho_{snow}$  are the snow depth in metres of water equivalent and snow density in  $\text{kg m}^{-3}$ , respectively.

In other respects, the sunglint parametrization of RTTOV is activated to describe the dependence of sunglint on the sea state, which is itself a function of 10-metre wind speed. The wave spectrum model of [Elfouhaily et al. \(1997\)](#) is preferred to that of [Yoshimori et al. \(1995\)](#), since the former yielded a slight reduction of reflectance biases against GOES-16 ABI in sunglint-affected regions (not shown).

Finally, it should be noted that the atlas of mean monthly land BRDF (Bidirectional Reflectance Distribution Function) of [Vidot and Borbás \(2014\)](#) is employed to specify snow-free land reflectances that are more realistic than RTTOV's default fixed value. Over snow-covered areas, the use of Eq.(3) and Eq.(4) instead of the monthly average reflectance values obtained from the BRDF atlas, allows to take into account the day-to-day variations of snow cover from the IFS.

### 2.3.3 Assumptions and limitations

In the current version of RTTOV/MFASIS used at ECMWF, cloud ice and snow are assumed to have the same optical properties and their respective contents are simply added before calculating the effective diameter of ice particles used in the radiative calculations. In the version of RTTOV employed in this study, ice particle effective radii are specified following [McFarquhar et al. \(2003\)](#) and resulting ice optical properties are parametrized according to [Baum et al. \(2011\)](#). For liquid water clouds, the Optical Properties of Aerosols and Clouds (OPAC) package of [Hess et al. \(1998\)](#) is selected. In the OPAC framework, four warm cloud types (convective or stratiform; over land or sea) are distinguished to specify effective particle radii and derive optical properties from cloud liquid water contents, assuming a modified gamma distribution for particle size. Furthermore, it is important to stress that ECMWF's current version of RTTOV/MFASIS ignores the influence of both molecular absorption and aerosols on reflectances. At the three investigated wavelengths, molecular absorption should be negligible, while the overall influence of aerosols is expected to remain small (less than 2% in reflectance) over the GOES FOV, except maybe in extreme situations over land (e.g., bio-mass burning in the Amazon basin during the dry season).

The version of MFASIS implemented in RTTOV v12.2 involves an eight-dimensional look-up table (LUT). The eight parameters of the LUT are: solar zenith angle  $\theta_{sun}$ , satellite zenith angle  $\theta_{sat}$ , scattering angle (i.e., the angle between incident and scattered directions), surface albedo, cloud liquid and ice optical depths and associated effective radii. As emphasized in [Scheck et al. \(2016\)](#), the use of an LUT does imply interpolation errors, which remain small for most situations. However, these errors can become particularly large for  $\theta_{sun}$  or  $\theta_{sat}$  above  $85^\circ$  (i.e., near sunrise/sunset or close to the edge of a geostationary satellite's FOV). Errors in such special conditions can be worsened by the fact that MFASIS operates on individual vertical profiles and thus cannot describe 3D radiative effects, such as those associated with cloud overlap, shadows and sloping cloud tops. Situations with zenith angles above  $85^\circ$  are therefore discarded from the statistical validation of IRM presented here.

A further limitation comes from the fact that in the version of MFASIS used here, Rayleigh scattering computations (1) only account for single scattering and (2) assume a fixed cloud top height for liquid water and ice cloud layers (4 and 8 km, respectively).

### 2.3.4 Outputs

The simulator outputs reflectances on a grid whose spacing varies linearly with satellite viewing angle. The resolution of this output grid is specified so as to match the resolution of operational deterministic forecasts (9 km) at sub-satellite point. The actual resolution (in km) of the output grid becomes coarser when satellite viewing angle increases (i.e., towards the limb).

## 2.4 Composite natural colour images

Throughout this study, various composite images obtained by combining reflectance factors ( $\rho$ ) in channels 1, 2 and 3, will be presented using data from both IRM and GOES-16 ABI. Reflectance factors are computed by multiplying reflectances with the cosine of  $\theta_{sun}$  (in other words,  $\rho = \kappa L_{\lambda}$ ; see Eq.(1)), in order to represent the natural dimming of the images towards the terminator. The specification of the Red/Green/Blue colour intensities (between 0 and 1) used to build the composite images follows Bah *et al.* (2018) as

$$\text{Red} = \rho_2; \quad \text{Green} = 0.45 \times \rho_1 + 0.45 \times \rho_2 + 0.1 \times \rho_3; \quad \text{Blue} = \rho_1 \quad (5)$$

Figure 1 displays an example of two composite natural colour images (a) as derived from GOES-16 ABI observations on 15 August 2021 1700 UTC and (b) as simulated by running RTTOV/MFASIS on the corresponding operational IFS 17h-range forecast (9-km resolution). The comparison of these two images already illustrates the fact that the overall agreement between IRM and GOES-16 ABI is better in the extratropics than in the tropics, as expected.

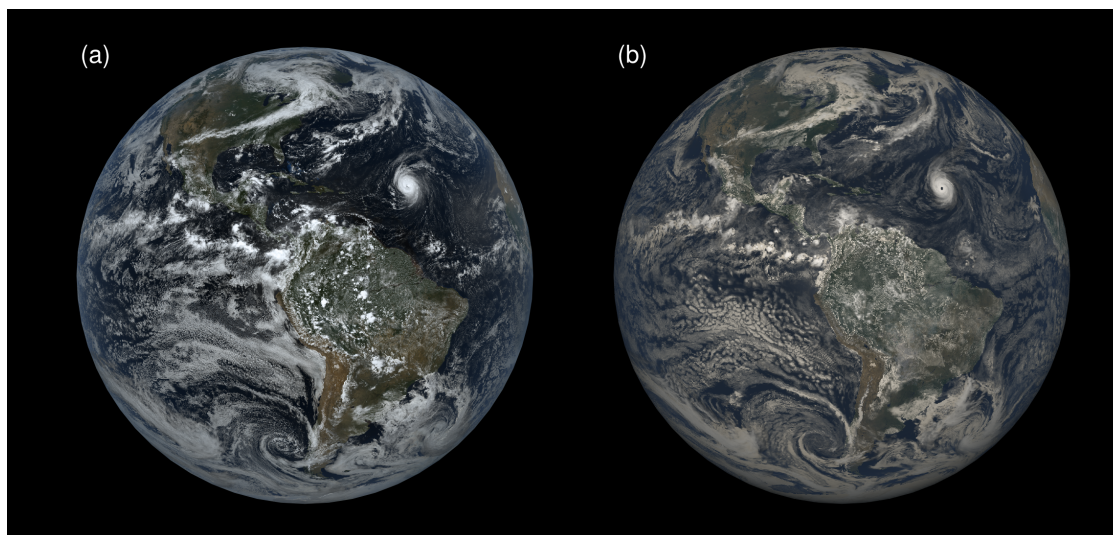


Figure 1: Example of composite natural colour images (a) observed by GOES-16 ABI on 20210905 1700 UTC and (b) simulated by running RTTOV/MFASIS on the corresponding operational IFS 17h-range forecast (9-km resolution). These images were created from reflectance factors in channels 1, 2 and 3, using Eq.(5).

## 3 Validation results

Before presenting statistical results of the validation, it is assumed that (1) errors in GOES-16 ABI reflectances (e.g., instrumental errors, geolocation errors) are small and (2) mismatches between IRM

and GOES-16 ABI reflectances originate from errors either in the RTTOV/MFASIS radiative transfer itself or in its input meteorological fields forecast by the IFS.

### 3.1 Background meteorology

To summarize the general circulation during each period of interest, first, Fig.2 displays maps of mean-sea-level pressure (MSLP) and total cloud cover averaged from daily operational IFS forecasts initialized at 0000 UTC, at hourly frequency up to the 24h-range for MSLP and at 17h range for total cloud cover. As expected, high pressures dominate inside the large anticyclones over subtropical oceans in both periods, as well as over North America in the winter (Fig.2a). The Southern Hemisphere (SH) anticyclones are stronger during the local winter (Fig.2b). This is particular true of the South Pacific High which extends towards the Chilean and Peruvian coasts. The usual wintertime strong dipole over the North Atlantic can easily be identified in Fig.2a. Low pressures dominate over southern polar regions as well as in the inter-tropical band, in both periods. In the latter region, the minimum of MSLP over the oceans is centered about the equator in Fig.2a, but displaced north of the equator in Fig.2b. Note that the high pressure values over the Andes are likely to be an artefact of uncertainties associated with below-ground extrapolation in the conversion of surface pressure to MSLP.

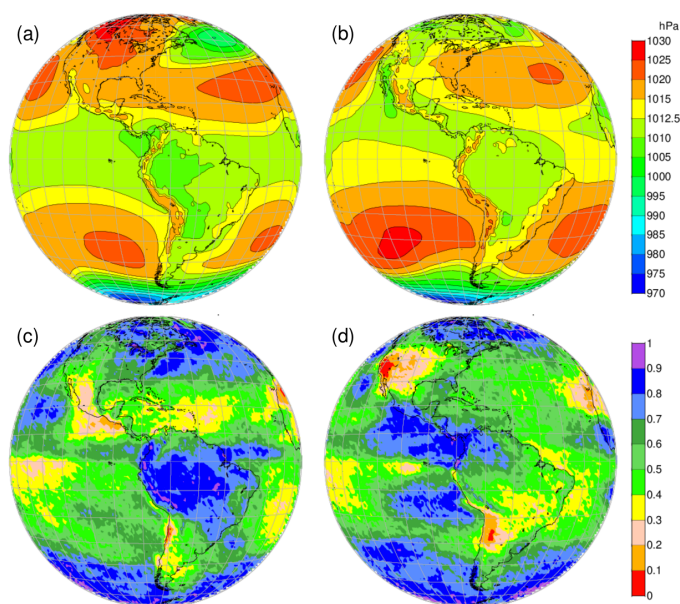


Figure 2: Mean-sea-level pressure (MSLP; in hPa; top panels) and mean total cloud cover (unitless; bottom panels) averaged over each of the two selected periods (a,c) 20210115-20210215 and (b,d) 20210815-20210915. Averaging has been applied to ECMWF’s operational daily forecasts started at 0000 UTC: hourly for MSLP and at 17h range for total cloud cover.

As far as total cloud cover is concerned, Fig.2c,d focuses on the valid time of 1700 UTC which corresponds to local noon at GOES-16 sub-satellite point, thereby maximizing the spatial coverage of solar spectrum data. Figure 2c,d offers a reminder of the predominance of clouds ( $> 0.7$ ) (1) over extratropical regions in both periods, (2) over the Amazon basin during the SH summer (rainy season), and (3) on the north-eastern flank of the South Pacific High (see Fig.2b) as well as over and west of Central America in the Northern Hemisphere (NH) summer. In contrast, low cloud cover ( $< 0.4$ ) dominates over (1) the Atacama Desert, (2) the south-west of North America, (3) North Africa and (4) the central equatorial Pacific (west of the domain).

## 3.2 Statistical analysis

### 3.2.1 Mean biases

Figure 3 displays maps of mean IRM–GOES-16 reflectance biases (expressed in units of reflectance) for channels 1, 2 and 3 and for the two selected periods. Only the validation time of 1700 UTC is presented here, since comparable signals were found at 1500, 1900 and 2100 UTC. While the biases for channels 2 and 3 (Fig.3c,d and Fig.3e,f, respectively) exhibit similar patterns of positive and negative values, channel 1 (Fig.3a-b) is affected by a widespread negative bias. IRM therefore systematically underestimates channel 1 reflectances. In fact, the bias for channel 1 can be seen as the superimposition of a “background” negative bias onto a bias similar to the one affecting the two other channels. To estimate this background negative bias of IRM in channel 1, Fig.4 displays differences in mean bias between channel 2 (resp. 3) and channel 1 for the boreal summer period. In other words, Fig.4 shows the respective differences (d)–(b) and (f)–(b) from Fig.3. Figure 4 confirms that the background bias in channel 1 is rather uniform in space (especially over oceans), with a mean value of about  $-6\%$  (in reflectance units). The uniform aspect in Fig.4 strongly suggests that the background bias in channel 1 originates from a deficiency in RTTOV/MFASIS rather than in the IFS model. The most likely explanation for this bias is that only single Rayleigh scattering is considered in the version of MFASIS used here. Since Rayleigh scattering is stronger at shorter wavelengths, channel 1 is much more affected than channels 2 and 3. The future inclusion of multiple Rayleigh scattering in MFASIS as part of RTTOV version 13 should significantly reduce the background bias (Saunders *et al.*, 2020). Other smaller contributions to the bias might come from the current specification of a fixed value of cloud top height in Rayleigh scattering computations (Scheck *et al.*, 2016), as well as from neglecting aerosols. The worsening of the negative differential bias towards the limb in Fig.4 supports the explanation involving Rayleigh scattering, since the latter is expected to increase with  $\theta_{sat}$  (i.e., for longer atmospheric paths above clouds).

In Fig.3, the most remarkable features common to all channels is the band of strong underestimation of reflectances by IRM (in red) along the north-eastern flank of the South Pacific High. The seasonal displacement of this anticyclone seen in Fig.2a,b is clearly reflected in Fig.3. In these regions, mean bias values usually lie between  $-10$  and  $-20\%$  (in reflectance units) in the NH winter period, and between  $-10$  and  $-30\%$  in the NH summer period (with even lower values just off the Peruvian coast). It was checked that the strong underestimation of reflectances by IRM off the western coast of South America during the NH summer is due to the frequent underprediction of low-level clouds by the IFS (not shown). Underestimations between  $-10$  and  $-20\%$  can also be found along the south-eastern flank of the North Pacific High, especially during the NH summer period (right column in Fig.3), as well as off the coast of West Africa in boreal winter (left column in Fig.3). In contrast, a clear overestimation of reflectances by IRM (in blue) affects the northern flank of the South Pacific High in boreal summer (right column in Fig.3). These pronounced positive and negative biases over tropical oceans highlight the fact that properly representing trade-wind low-level clouds remains one of the greatest challenges for the IFS, and more generally, for all NWP and climate models (e.g., Nuijens *et al.*, 2015). One should note that consistent IFS biases over this region were already evidenced at shortwave frequencies by Ahlgrimm *et al.* (2018), but also at microwave frequencies by Kazumori *et al.* (2016) (their figures 15 and 16). The issues affecting simulated clouds over tropical oceans will be further investigated in section 3.3.2.

Another noticeable signal in Fig.3 is the marked underestimation of reflectances in all three channels very close to the limb. Note that at Fig.3’s valid time of 1700 UTC, Earth’s limb, as viewed from the GOES satellite, almost coincides with the terminator. In fact, bias maps for 1500, 1900 and 2100 UTC (not shown) indicate that this negative bias is mainly associated with large values of  $\theta_{sun}$  (i.e., close to the terminator). Scheck *et al.* (2016) showed that the current MFASIS LUT can be too coarse to guarantee an

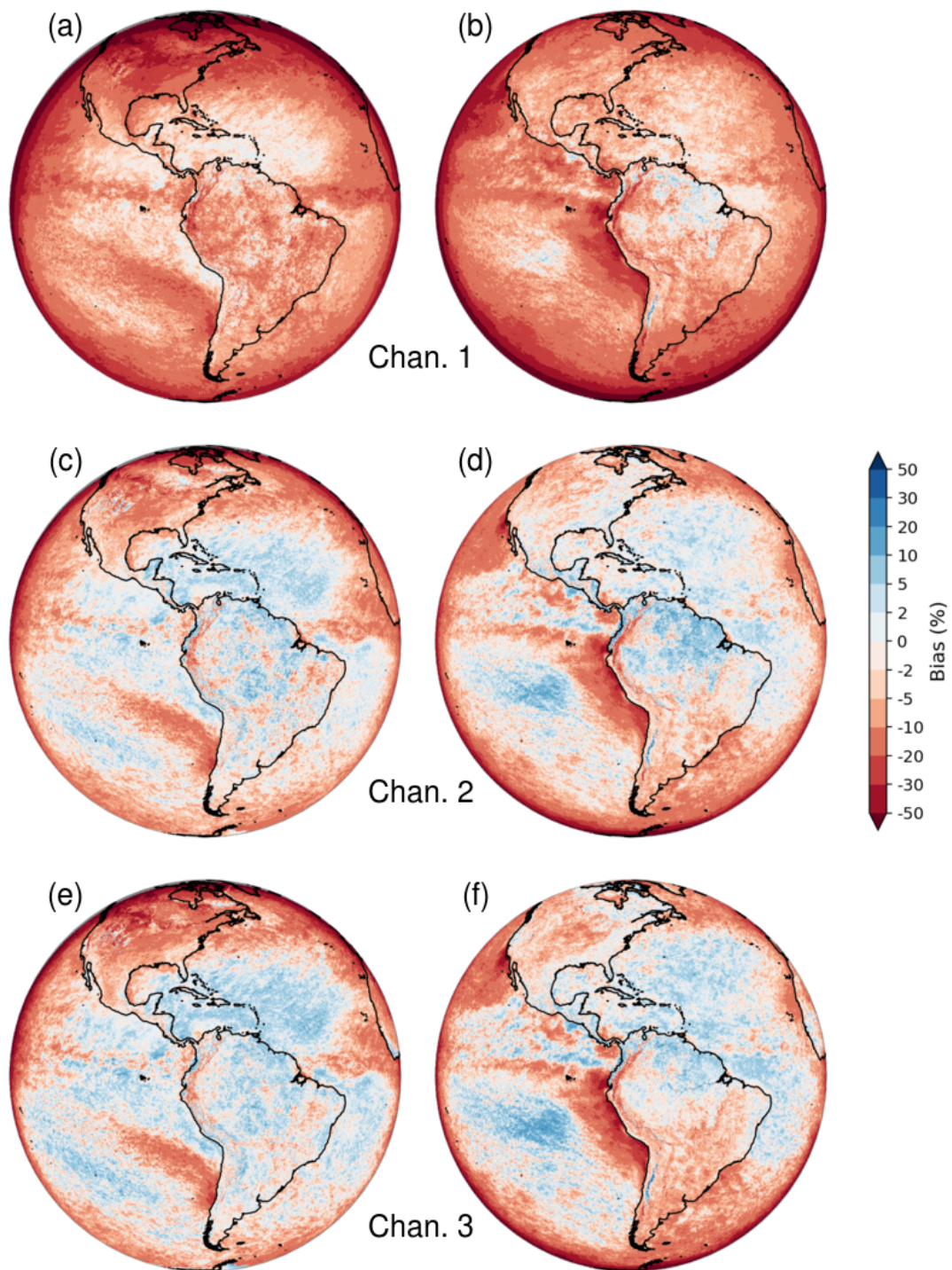


Figure 3: Mean IFS+RTTOV/MFASIS–GOES-16 ABI reflectance bias over the two selected periods: 20210115-20210215 (left column) and 20210815-20210915 (right column) and for IFS forecast range +17h (sub-satellite local noon). Channels 1, 2 and 3 are displayed on the top, middle and bottom rows, respectively. Bias is expressed in units of reflectance (percent).

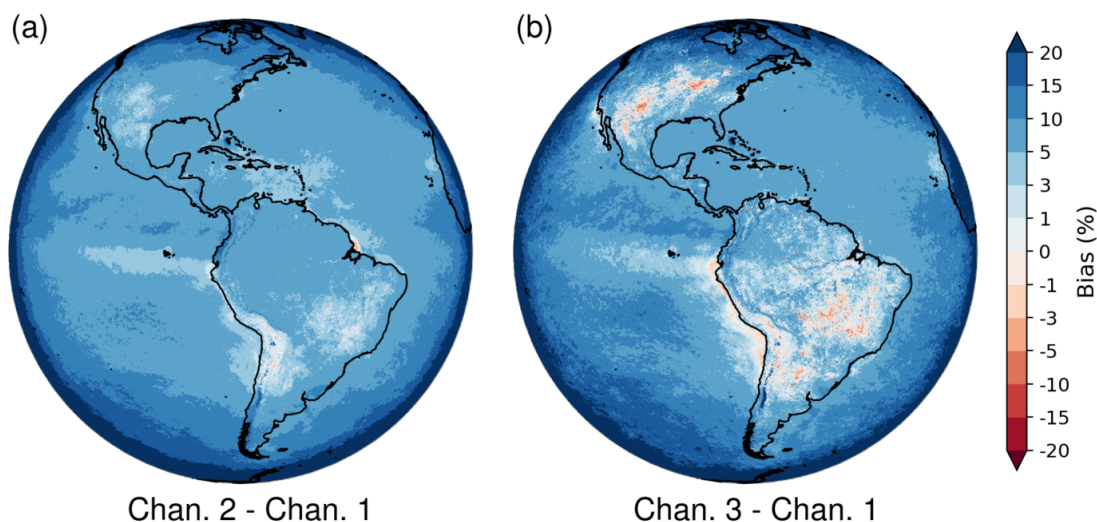


Figure 4: Mean IFS+RTTOV/MFASIS–GOES-16 ABI reflectance bias difference for (a) channel 2 minus channel 1 and (b) channel 3 minus channel 1, over the period 20210815-20210915 and for IFS forecast range +17h (sub-satellite local noon). These maps highlight the background negative bias which affects channel 1, especially over oceans. Bias difference is expressed in units of reflectance (percent).

accurate interpolation of input cloud parameters for large zenith angles, causing higher reflectance errors. Even though IRM reflectances for  $\theta_{sun} > 85^\circ$  are already discarded from our statistics, Fig.3 suggests that this rejection criterion should be extended to  $\theta_{sun} > 80^\circ$ . This is confirmed in the latest validation of MFASIS presented in Scheck (2021). This tighter criterion would be particularly crucial in future data assimilation applications. In contrast, the other exclusion criterion  $\theta_{sat} > 85^\circ$  seems to be sufficient.

The north of the Amazon region is characterized by an overestimation of reflectances in IRM, which can reach 10% locally, especially during the NH summer (Fig.3b,d). This issue will be further investigated in section 3.3.3. Finally, a negative bias around  $-10\%$  affects the central United States and western Canada during the winter period (Fig.3a,c,e). Determining the exact origin of this particular bias would require some validation against other types of observations, which is beyond the scope of this study.

### 3.2.2 Frequency distributions

Frequency distributions of reflectances from IRM and GOES-16 ABI are compared in Fig.5 for the period 20210815-20210915, with a distinction between land and sea. Frequency distributions for the other period do not yield more information and are therefore not shown here. For GOES ABI observations, the peak in the frequency distribution over land occurs for reflectances around 15-18% for channels 1 and 2, and around 40% for channel 3. This difference is due to the much higher sensitivity of the latter channel to vegetation. Over sea, the peak occurs at a reflectance value around 15% in channel 1, and 4-6% in channels 2 and 3.

The overall shapes of the frequency distributions for IRM and GOES ABI agree fairly well. However, for all three channels, IRM underestimates the occurrence of the higher reflectances, especially above 80%, which are typically associated with thick cloud situations. This underestimation is strongest for channel 1 over sea (Fig.5b), which is consistent with the much larger mean biases already identified in Fig.3a,b. Several reasons might explain this inability of IRM to produce high enough reflectances from

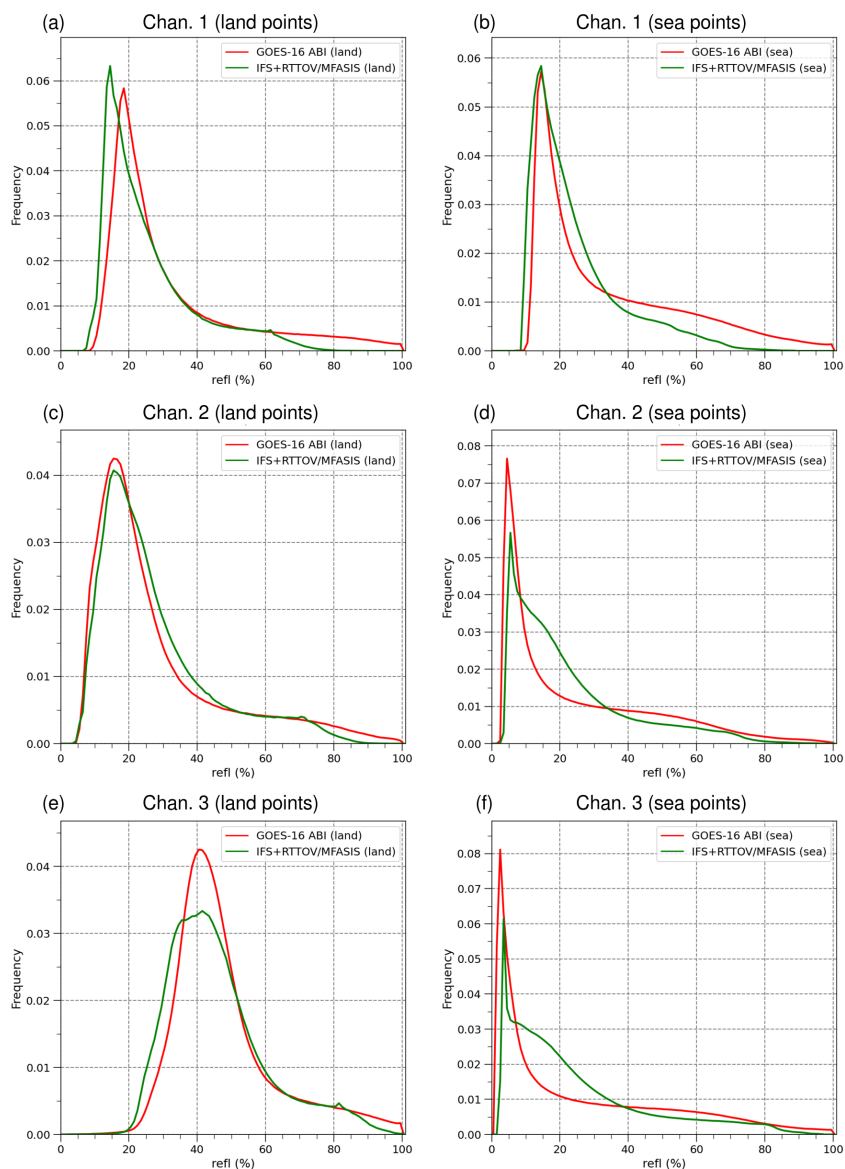


Figure 5: Frequency distributions of IFS+RTTOV/MFASIS and GOES-16 ABI reflectances for channels 1, 2 and 3 (top to bottom) over land (left) and sea (right), for the period 20210815-20210915. Valid time is 1700 UTC (sub-satellite local noon).

thick clouds:

- Inadequacies in the specification of cloud liquid water and ice radiative properties (e.g., effective radius) in RTTOV/MFASIS.
- The non-inclusion of convective hydrometeors in offline RTTOV/MFASIS computations (personal communication from Liam Steele of ECMWF), since these 3D diagnostic fields are currently not archived in IFS operational forecasts.
- The fact that the sub-grid scale variability of model fields is ignored in RTTOV/MFASIS.

### 3.2.3 Correlations

While biases presented in section 3.2.1 can be affected by both radiative transfer deficiencies and IFS modelling errors, correlations are likely to be mainly determined by how similar clouds look between IRM and GOES-16 ABI, in terms of their shape, size and location. Figure 6 shows maps of the reflectance correlations for the two selected periods. Only channel 2 and validation time 1700 UTC are presented here, since the two other channels and other times of the day exhibit very similar patterns. For both periods, correlations are above 0.6 over most extratropical regions, while they are usually below 0.2 in tropical regions, especially over the Pacific Ocean and over the Amazon basin. This worse agreement between IRM and observations in the tropics is to be expected, due to the challenges in forecasting deep convection (e.g., over the Amazon basin) as well as trade-wind clouds over tropical oceans (as already mentioned in section 3.2.1). A further analysis of these tropical deficiencies will be proposed in section 3.3 by looking at individual situations.

In Fig.6b, three regions with correlations above 0.7 are associated with the footprints of the three major hurricanes Larry (narrow band stretching across the tropical North Atlantic), and Grace and Ida (Caribbean Sea and south-eastern United States). These NH summer patterns illustrate the fact that in the tropics, the IFS is more skilful at predicting the distribution of clouds inside intense storms than in quieter situations, with weak pressure gradients.

Finally, the poor correlations over the Canadian Arctic in Fig.6a are likely due to MFASIS's known inaccuracies at very low sun elevations, while the low correlations over the Atacama Desert (Andes) in Fig.6b are an artefact of the extremely low day-to-day variability of reflectances in quasi-permanent clear-sky conditions. In such situations, tiny differences in reflectance between IRM and GOES-16 may cause a spurious large drop in the correlation coefficient.

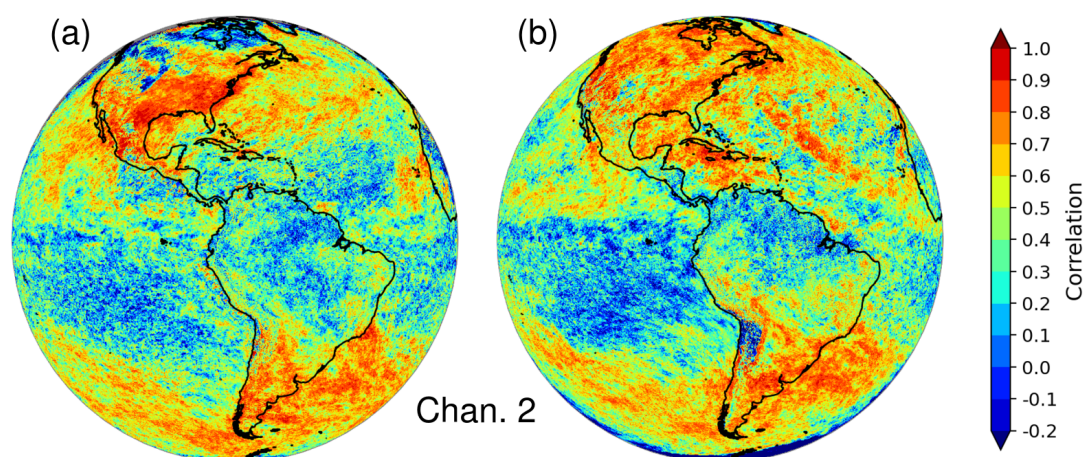


Figure 6: IFS+RTTOV/MFASIS versus GOES-16 ABI reflectance correlation for channel 2 over the two selected periods: 20210115-20210215 (left column) and 20210815-20210915 (right column), for IFS forecast range +17h (sub-satellite local noon). Channels 1 and 3 are not shown because the maps look very similar to those for channel 2.

3.2.4 Standard deviation ratios

Figure 7 displays maps of the reflectance standard deviation ratio  $SDR = \sigma_{IRM} / \sigma_{GOES}$  for channels 1, 2 and 3 and for the two periods. Again, only time 1700 UTC is shown here, as other times exhibit similar patterns. For channel 1,  $SDR$  is usually well below unity. In other words, the variability of reflectances tends to be smaller for IRM than for GOES ABI. This widespread reduction of variability for channel 1 can be explained by the systematic negative background bias that was highlighted in Fig.4. Indeed, this bias is accompanied by a systematic flattening of IRM’s reflectance range compared with GOES’s. In contrast,  $SDR$  is much closer to unity for channels 2 and 3, which underlines the similarity of day-to-day variations of reflectance in IRM and GOES ABI. Values of  $SDR$  below 0.5 are mainly found over tropical oceans, especially near the equator for both periods, while values above 1.5 are mainly concentrated over eastern Brazil and northern Argentina in the NH summer (Figure 7.d,f). Again, as for the correlations in section 3.2.3, the patch of very low  $SDR$  over the Atacama Desert during the NH summer (Figure 7.d,f) cannot be considered as significant due to the extremely low day-to-day variability of reflectances.

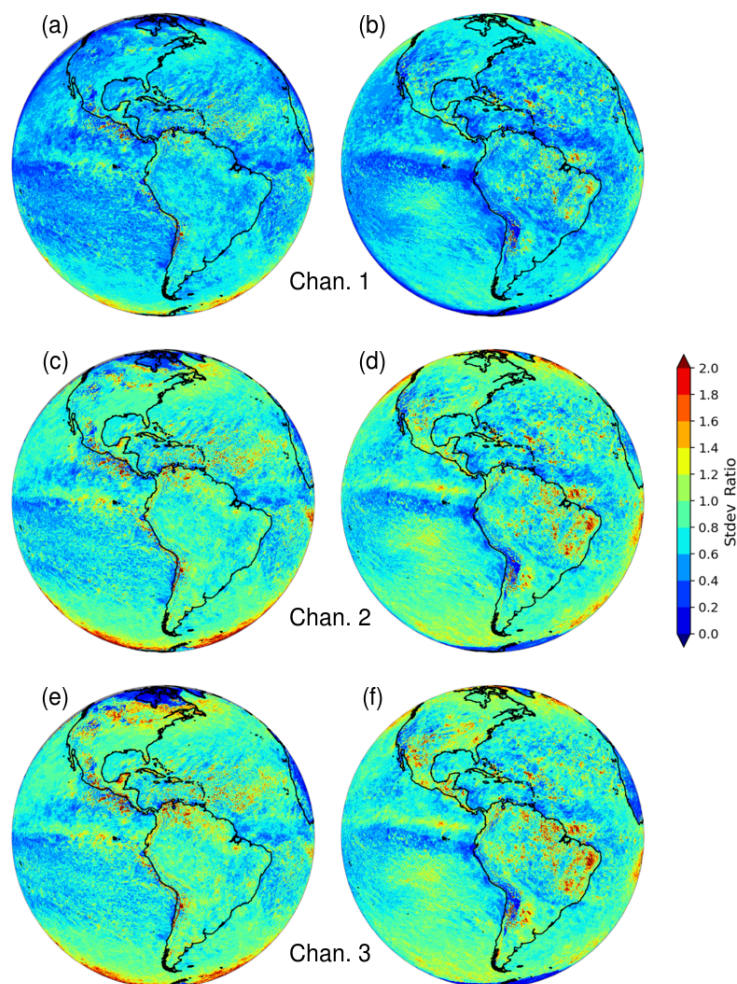


Figure 7: Mean IFS+RTTOV/MFASIS / GOES-16 ABI reflectance standard deviation ratio over the two selected periods: 20210115-20210215 (left column) and 20210815-20210915 (right column) and for IFS forecast range +17h (sub-satellite local noon). Channels 1, 2, 3 are displayed on the top, middle and bottom rows, respectively.

### 3.3 Specific aspects

#### 3.3.1 Sunglint

In addition to the general biases presented in section 3.2.1, an evaluation of how well sunglint effects are simulated in RTTOV/MFASIS (see section 2.3) is carried out. To this end, the mean IRM–GOES-16 reflectance bias is stratified against  $\varepsilon$ , which is defined as the angle between the view vectors (satellite to point on Earth) of the centre of the sunglint region, and the selected point on Earth. For instance,  $\varepsilon = 0^\circ$  means that the point of interest coincides with the location of maximum sunglint on Earth’s surface. The resulting bias curves for each channel are shown in Fig.8 based on forecasts initialized at 0000 UTC and valid at 1900 UTC. Note that the time of 1900 UTC was chosen (rather than 1700 UTC) to ensure the occurrence of sunglint over the Pacific Ocean. First, Fig.8 confirms the results of Fig.3, namely the systematic negative bias in channel 1 reflectances (around  $-6\%$ ) and the overall smaller biases in channels 2 and 3. For  $\varepsilon$  above  $6^\circ$ , the stronger negative biases in all channels are due to MFASIS errors for large zenith angles (see section 2.3.3). More interestingly, the bias for all three channels clearly increases when  $\varepsilon$  decreases from  $2^\circ$  to  $0^\circ$ , which suggests that RTTOV might overestimate reflectances in sunglint-affected regions by about 7 to 10% on average. As already mentioned in section 2.3.2, the wave spectrum model of [Elfouhaily et al. \(1997\)](#) (used here) led to slightly smaller biases than [Yoshimori et al. \(1995\)](#)’s (not shown).

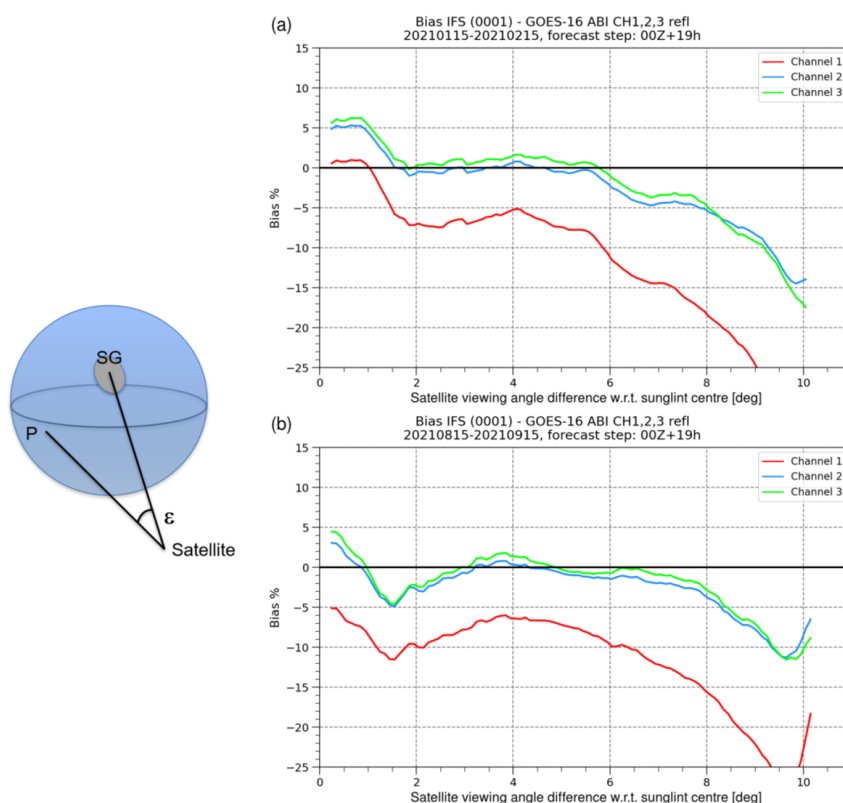


Figure 8: Mean IFS–GOES-16 ABI reflectance bias as a function of the satellite viewing vector angle relative to the centre of the sunglint region,  $\varepsilon$  (in degrees; see illustration on the left), for (a) 20210115-20210215 and (b) 20210815-20210915 and for IFS forecast range +19h (i.e., sub-satellite 14:00 local time).  $\varepsilon$  is equal to zero when the point of interest  $P$  on Earth’s surface coincides with the centre of the sunglint region (SG). Curves are shown for channels 1, 2 and 3 (see legend).

3.3.2 South Tropical Pacific low-level clouds

The two natural colour images shown in Fig.9 offer a further insight into the mis-representation of low-level clouds over the tropical South Pacific Ocean in the IFS, which was already inferred from mean statistics in section 3.2. Figure 10 displays a vertical cross-section of IFS clouds along latitude 16°S, which indicates that the simulated low-level cloud deck gradually rises between 75°W and 90°W from about 1000 m to 1600 m (model levels 118 to 113), before levelling off. First, one should note that the

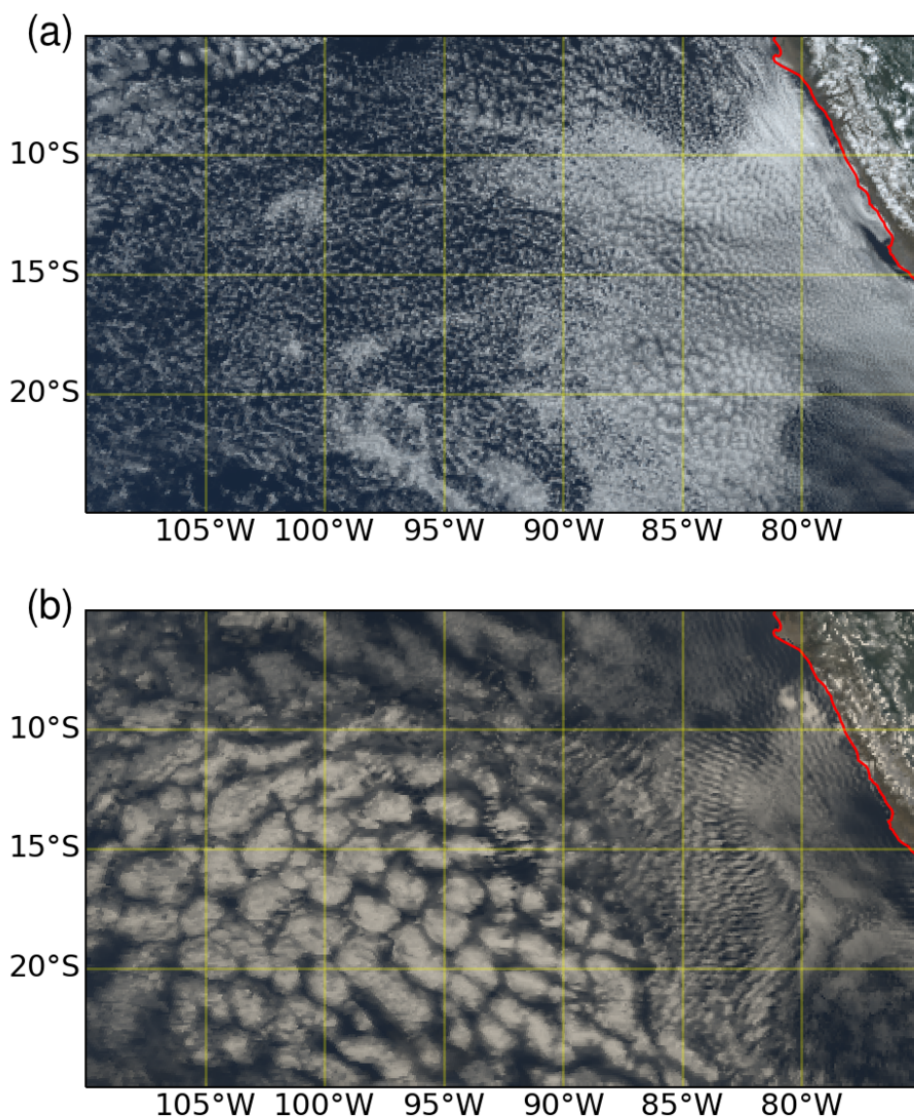


Figure 9: Comparison of (a) GOES-16 ABI and (b) IFS+RTTOV/MFASIS natural colour images over the tropical South Pacific on 20210909 1700 UTC. The simulated image was obtained using the operational IFS 17h-range forecast from 0000 UTC. Both simulated and GOES images are shown at 9-km resolution.

more yellowish hue in the simulated image (Fig.9b) is likely due to the widespread negative bias in channel 1 (e.g., see Fig.3a-b). Besides, Fig.9b clearly shows that west of 88°W, the low-level clouds produced by the IFS tend to cluster on a scale of typically 180 km, while those observed by GOES (Fig.9a) exhibit

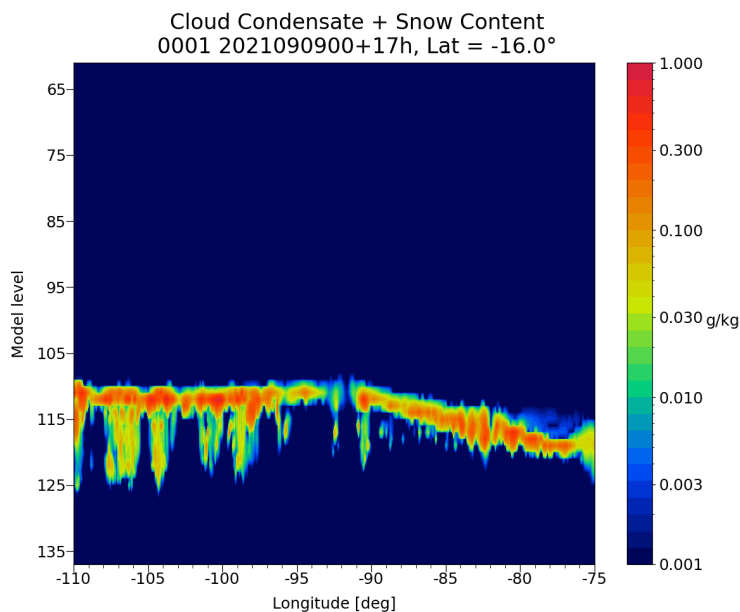


Figure 10: Cross-section of cloud condensate plus snow contents along latitude  $16^{\circ}\text{S}$  across the domain of Fig.9b on 20210909 1700 UTC, from the operational IFS 17h-range forecast (9 km resolution). The vertical axis shows model levels from 61 ( $\approx 16\text{-km}$  altitude) to 137 (surface).

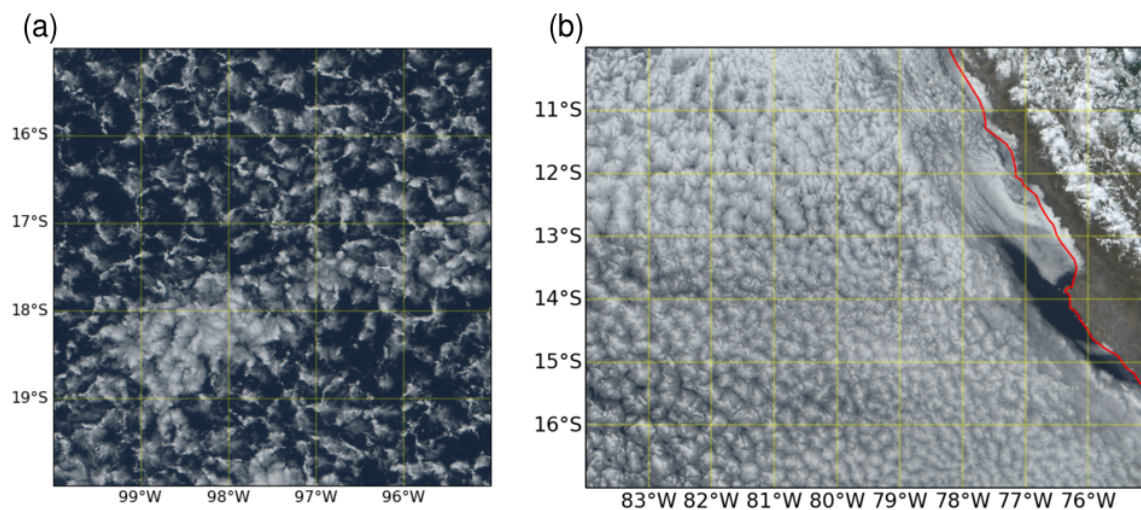


Figure 11: Two zooms (at 1-km resolution) applied to the GOES-16 ABI natural colour image shown in Fig.9a.

much smaller horizontal scales. Indeed, Fig.11a, which shows a zoom at 1-km resolution on the central region of the GOES image in Fig.9a, reveals that open-cell convection dominates in the real world, with typical cloud sizes ranging between 2 and 20 km. Even though the 9-km resolution of operational IFS forecasts precludes the proper representation of such small scales, the predicted cloud size does seem overly large. It seems worth mentioning that a 66h-range IFS forecast run at 2.9 km resolution for a

different date still suffered from the same overestimation of cloud size over the same region (not shown). The inability of the IFS to simulate open-cell convection might indicate an inadequate interaction between the model's physics and dynamics. Another contributing factor might be the missing influence of precipitation on the formation and evolution of open cells in the model, including the possible modulation by aerosols, as advocated by Feingold *et al.* (2010), for instance. Interestingly, Fig.12 displays a zoom of simulated channel 2 reflectances over a subdomain where large cloud cells dominates in the IFS, together with the corresponding field of vertical velocity on model level 114 (i.e., near cloud base), on 20210909 1700 UTC. Fig.12 shows that the simulated reflectances are almost perfectly anticorrelated with vertical velocity (expressed in  $\text{Pa s}^{-1}$ ) at cloud base, which confirms that the dynamical forcing in the IFS is too wide-scale.

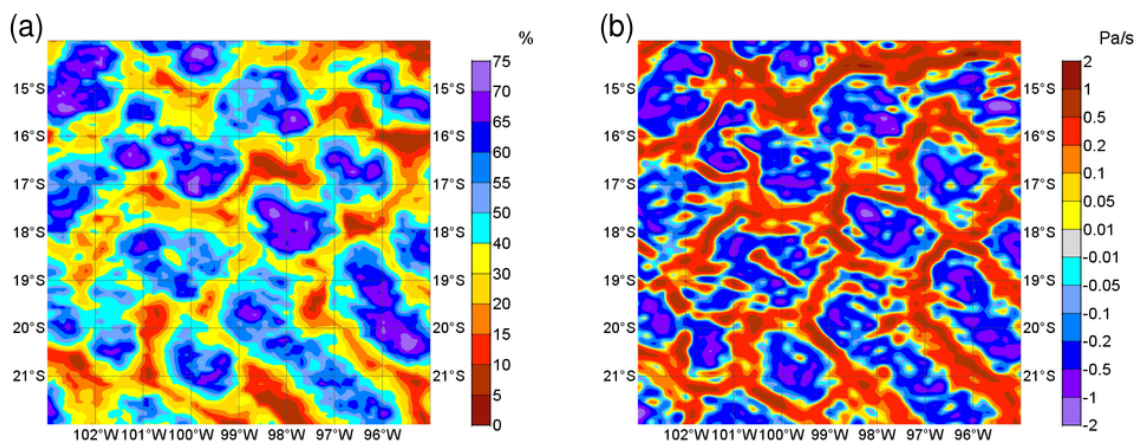


Figure 12: Zooms over subdomain  $[103^{\circ}\text{W}/95^{\circ}\text{W}; 22^{\circ}\text{S}/14^{\circ}\text{S}]$  (tropical South Pacific Ocean) on 20210909 1700 UTC: (a) simulated channel 2 reflectances and (b) vertical velocity on model level 114 (near cloud base; in units  $\text{Pa s}^{-1}$ ). Positive (resp. negative) vertical velocity values indicate descent (resp. ascent). Both plots were produced using the operational 17h-range IFS forecast.

The frequent occurrence of these unrealistically large cloud cells in the IFS over the western half of Fig.9b, can be verified in Fig.13. This figure shows a comparison of the mean power spectra computed from the red component of simulated and observed natural colour images over the period 20210815-20210915 and over the subdomain  $[106^{\circ}\text{W}/89^{\circ}\text{W}; 25^{\circ}\text{S}/10^{\circ}\text{S}]$ . Note that spectra for the green and blue components of the images would look very similar (not shown). When compared with its GOES counterpart, the mean power spectrum derived for IRM images exhibits a very clear bulge for spatial scales between 150 and 200 km (and lower power for smaller scales), thereby confirming that overly large cloud clusters are a common feature in the IFS.

In contrast, between  $88^{\circ}\text{W}$  and the South American coast, the typical scales of simulated and observed clouds in Fig.9 are more comparable, but the IFS tends to substantially underestimate cloud amounts. According to 1-km resolution GOES observations (Fig.11b), the latter region is dominated by a gradual westward transition from stratocumuli to closed-cell convection.

Overall, these findings are consistent with the bias dipole found in Fig.3d,f, with positive (resp. negative) values over the western (resp. eastern) part of the domain of Fig.9.

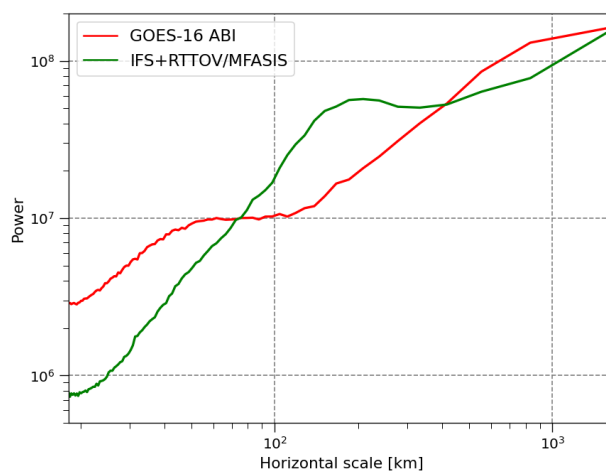


Figure 13: Mean power spectra of the red component of natural colour images from simulations (green curve) and from GOES-16 observations (red curve) over the period 20210815-20210915 and over subdomain [106°W/89°W; 25°S/10°S] (tropical South Pacific Ocean). The valid time is 1700 UTC and daily 17h-range IFS forecasts have been used.

### 3.3.3 Amazonian convection

Figure 14 displays observed and simulated natural colour images valid at 1700 UTC and 1900 UTC (i.e., local noon and 2pm, respectively) on 20210909 over the Amazon region. While convective activity

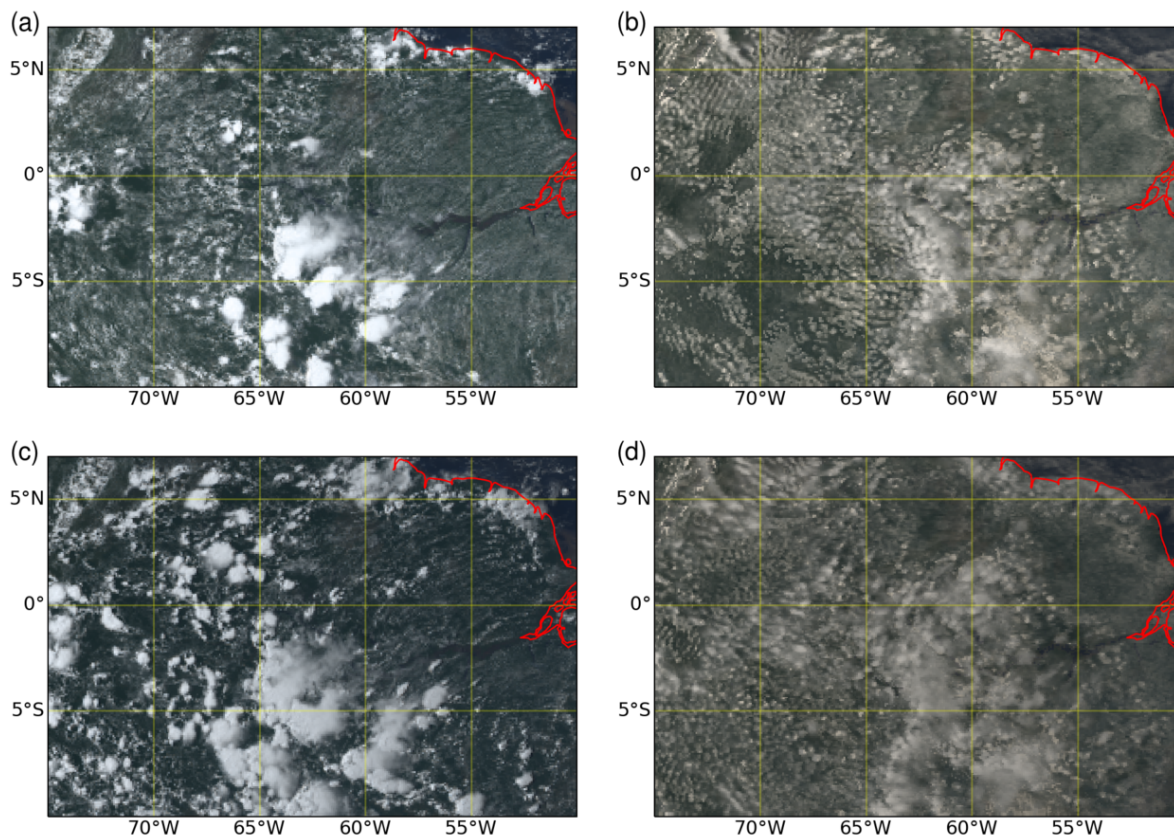


Figure 14: Comparison of GOES-16 ABI (left panels) and IFS+RTTOV/MFASIS (right panels) natural colour images over the Amazon region on 20210909 at 1700 UTC (top row) and 1900 UTC (bottom row). The simulated images were obtained using operational IFS 17h and 19h-range forecasts from 0000 UTC. Both simulated and GOES images are displayed at the same resolution as IRM (9 km).

dominates in both GOES observations and IRM as expected, reflectance patterns associated with clouds look rather different. Both satellite images (Fig. 14a,c) exhibit several large convective cloud clusters that are well-structured, whose typical size is above 100 km and which tend to spread horizontally between 1700 (panel a) and 1900 UTC (panel c). The IFS model does predict substantial convective activity at the right place, but the highest reflectance values computed by IRM are substantially lower than those observed. The systematic underestimation by IRM of reflectances above 70% in thick-cloud scenes was already underlined by the frequency distributions shown in Fig. 5. At 1900 UTC, around the centres of deep convection, shallower cumulus clouds remain omnipresent in the model (Fig. 14d), but have almost disappeared in the GOES image (Fig. 14c). The tendency of the IFS to over-predict the occurrence of shallow convection over the Amazon domain is confirmed by mean spectra computed at 1900 UTC in Fig. 15, with higher spectral power at scales between 30 and 50 km in IRM than in GOES images. It is worth noting that the NH summer period (dry season in the Amazon region) turns out to be much more affected by the shallow convection overestimation than the NH winter period (rainy season).

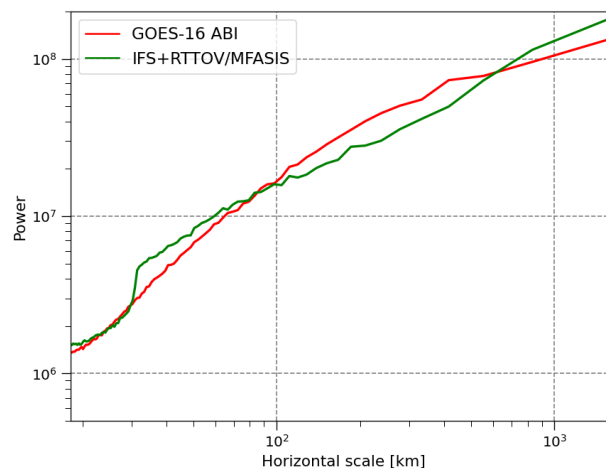


Figure 15: Mean power spectra of the red component of natural colour images from simulations (green curve) and from GOES-16 observations (red curve) over the period 20210815-20210915 and over subdomain [70°W/55°W; 10°S/5°N] (Amazon region). The valid time is 1900 UTC and daily 19h-range IFS forecasts have been used.

### 3.3.4 Tropical cyclones

Observed and simulated natural colour images of major hurricane Larry for three consecutive days at 1700 UTC are displayed in Fig. 16. First, this figure illustrates the IFS's ability to predict Larry's location and overall structure quite accurately for the selected 17h forecast range. The model is even capable of properly representing the main spiralling cloud bands and the size of the simulated eye agrees well with GOES observations. One noticeable discrepancy is the total absence of clouds inside the eye in the simulated images (dark central spot in Fig. 16b,d,f), on all three days. In Fig. 17, the comparison of full-resolution zooms from GOES-16 ABI (a) visible channel 2 and (b) infrared channel 14 over hurricane Larry's core on 20210906 1700 UTC, highlights the low-level nature of the clouds inside the particularly large eye (bright in channel 2, dark in channel 14).

The lack of simulated clouds in the eye is also exemplified in Fig. 18, which displays images from GOES-16 ABI (top) and from IRM 66h-range simulations (bottom) of major hurricane Irma, valid on 20170908 1800 UTC. Irma's dark eye in GOES-16 ABI infrared channel 14 in Fig. 18b confirms that the high solar reflectances found inside the eye in Fig. 18a must be due to low-level clouds. Furthermore, the IRM image based on data from an experimental IFS forecast at 2.9-km resolution in Fig. 18d suffers from the same lack of low-level clouds inside the eye. One possible explanation would be that the subsidence inside the eye is too strong in the IFS, thereby preventing cloud formation.

Finally, Fig. 19 compares frequency distributions of GOES-16 ABI and IRM channel-2 reflectances focusing on hurricane Larry's core, accumulated over the three consecutive days shown in Fig. 16. The distribution of reflectances above 60% is clearly shifted to the left in IRM, with reflectance values above 90% being inexistent in the simulations, but very common in the observations. This shift is consistent with the more general underestimation of the higher reflectances of thick clouds with IRM, as already evidenced in Fig. 5 and Fig. 14.

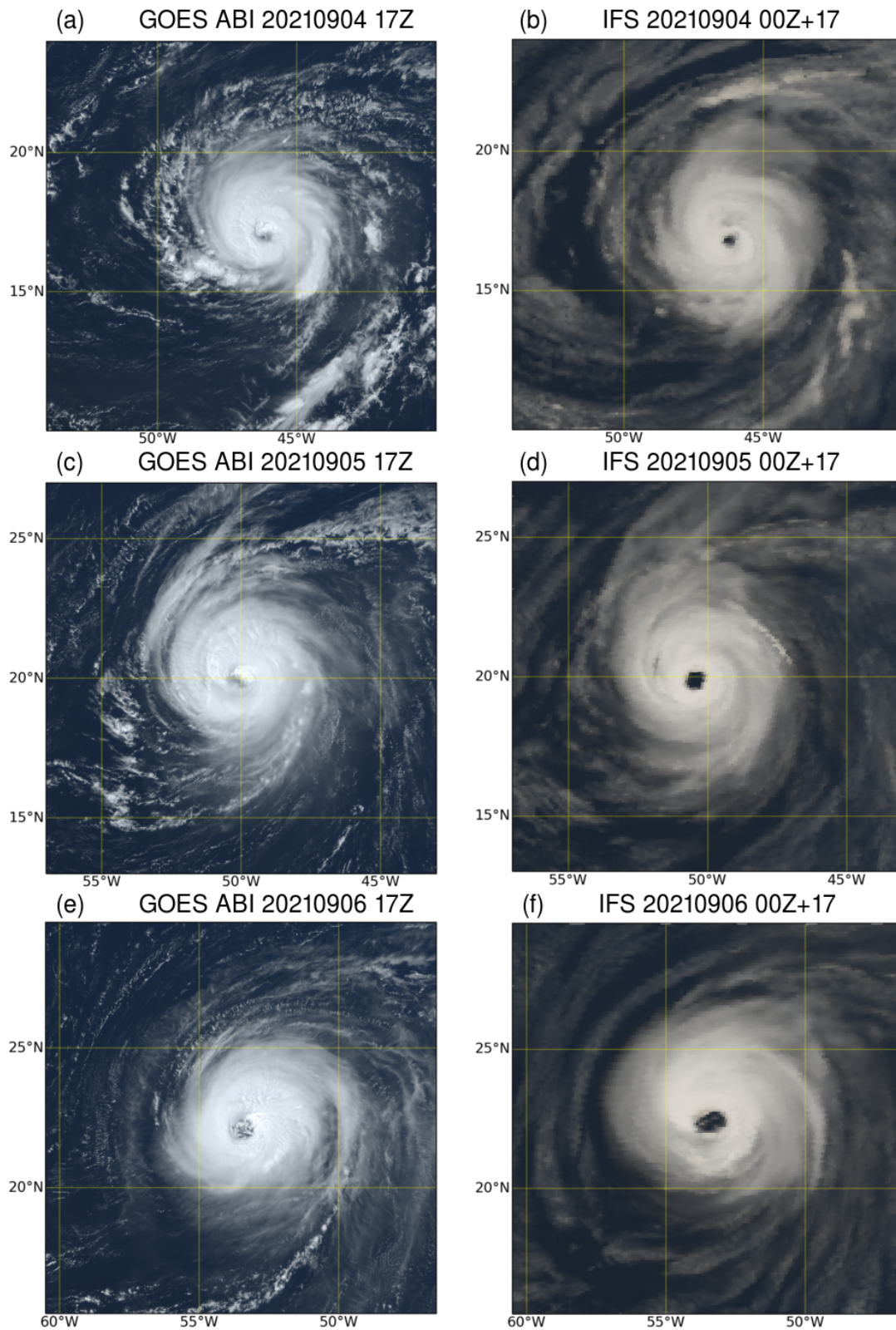


Figure 16: Comparison of GOES-16 ABI (left panels) with IFS+RTTOV/MFASIS (right panels) natural colour images of hurricane Larry on 20210904, 20210905 and 20210906 1700 UTC (resp. top, middle and bottom row). Simulated images are based on operational IFS 17h-range forecasts (9-km resolution). GOES images have a 1-km resolution.

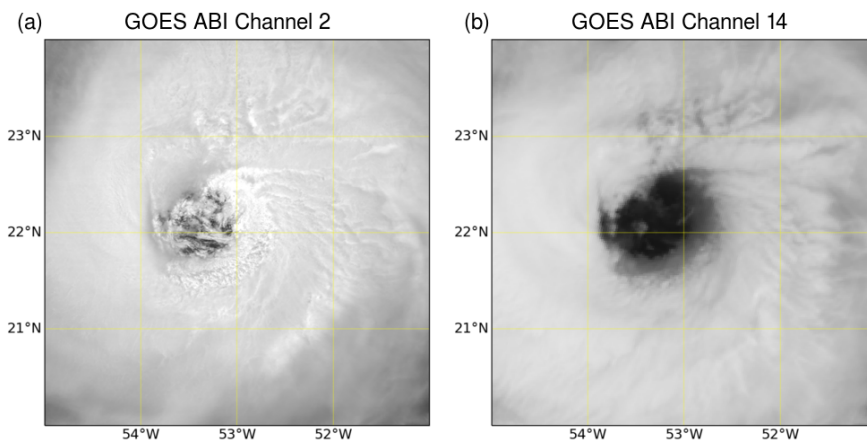


Figure 17: Full-resolution zooms over hurricane Larry's core on 20210906 1700 UTC from GOES-16 ABI: (a) visible channel 2 and (b) infrared channel 14. Image resolution is 0.5 and 2 km, respectively.

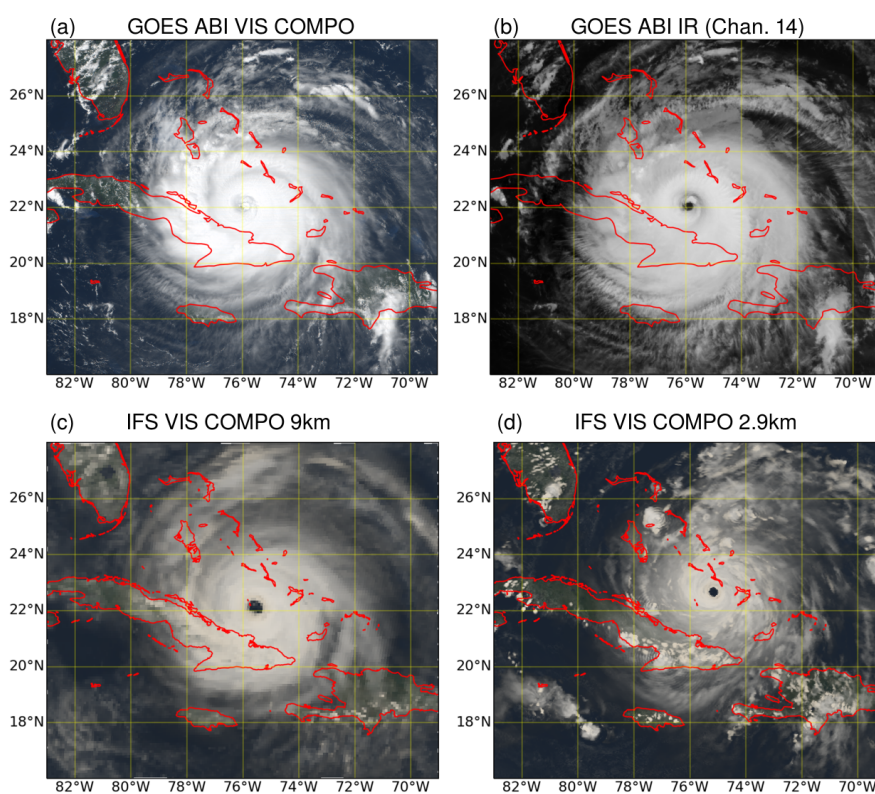


Figure 18: Hurricane Irma on 20170908 1800 UTC: GOES-16 ABI (a) natural colour image and (b) channel 14 infrared brightness temperatures; (c,d) IFS+RTTOV/MFASIS natural colour images simulated from 66h-range forecasts at 9 and 2.9-km resolution, respectively (initialized at 0000 UTC). GOES images in (a) and (b) are at 1-km and 2-km resolution, respectively.

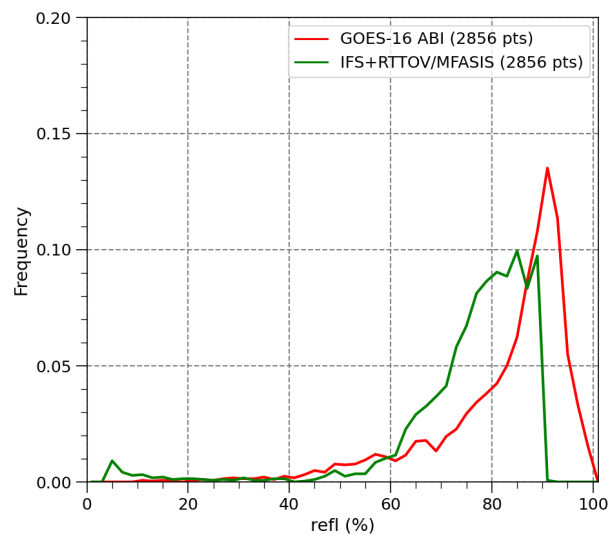


Figure 19: Frequency distributions of GOES-16 ABI and IFS+RTTOV/MFASIS channel-2 reflectances over hurricane Larry's core, using data from 4, 5 and 6 September 2021 at 1700 UTC. For each date, distributions have been computed inside a  $3^\circ \times 3^\circ$  window centered about the storm's eye. Simulated reflectances are based on operational IFS 17h-range forecast data.

### 3.4 Additional validation using CERES data

To support the above findings from the validation of IRM against GOES-16 reflectances, IFS forecast top-of-atmosphere net broadband shortwave fluxes (TOA-BSWF; positive downwards) are compared with observations from CERES (Clouds and the Earths Radiant Energy System; Doelling *et al.*, 2013). These observations come from the SYN1deg product obtained from NASA<sup>3</sup> CERES's website <https://ceres.larc.nasa.gov/data>. In SYN1deg, daily 1-degree resolution TOA-BSWF data are generated by combining solar spectrum radiances from CERES instruments on board several low-earth-orbit sun-synchronous satellites (Terra, Aqua, Suomi-NPP and NOAA-20), as well as from geostationary satellites (to fill gaps between CERES orbits). One should note that the SYN1deg TOA-BSWF product cannot be considered as completely independent data here, since by construction, it is partially based on GOES-16 solar spectrum radiance observations. One interesting aspect of the validation against CERES is that it does not involve RTTOV/MFASIS.

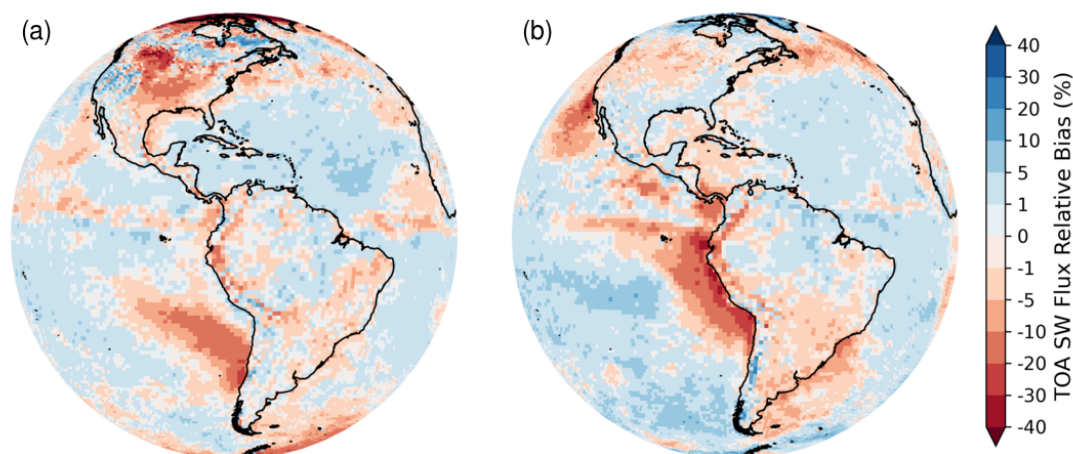


Figure 20: Daily mean CERES–IFS relative difference (in %) in net broadband shortwave fluxes at the top of the atmosphere, over the periods (a) 20210115–20210215 and (b) 20210815–20210915, and over the GOES-16 field of view.

Figure 20 presents the daily average TOA-BSWF relative bias between CERES and the IFS over the two selected periods. Even though Fig.20 is based on mean daily TOA-BSWF while Fig.3c,d was based on channel-2 reflectances at 1700 UTC, the respective signals look remarkably similar, away from the limb. This supports the idea that the bias in the central region of the GOES-16 FOV are mainly caused by deficiencies in the IFS. In contrast, near the limb, the absence of a ring of negative bias values in Fig.20 compared with Fig.3c,d confirms that this signal mainly originates from the Rayleigh scattering issue in RTTOV/MFASIS, as described in section 3.2.1. In the outer regions of the FOV, however, the substantial negative bias over North America in winter cannot be attributed to RTTOV/MFASIS, since it appears on both Fig.20a and Fig.3c. The same is true for the negative bias off the coast of Baja California in the summer, in Fig.20b and Fig.3d.

<sup>3</sup>National Aeronautics and Space Administration (USA)

## 4 Summary and conclusions

A validation of solar reflectances simulated by running RTTOV/MFASIS on IFS operational short-range forecast data (at 9-km resolution) against GOES-16 ABI reflectances in channels 1, 2 and 3 has been carried out over two 1-month-long periods. The choice of GOES rather than MSG (Meteosat Second Generation) observations was motivated by the easier access to the GOES data and by the fact that a similar validation against GOES-17 (overlooking the central Pacific) would be straightforward. Performing such assessment for visible and near-infrared channels provides a novel insight into the performance of IFS+RTTOV/MFASIS, which confirms or complements the results from previous validation exercises based on infrared and microwave channels. In particular, visible frequencies allows the study of low-level clouds, which are often hard to detect in infrared window channels. The findings from this study might also be useful for the planned assimilation of solar reflectances in ECMWF's 4D-Var system (quality control; observation screening), should MFASIS be selected as the visible reflectance observation operator. They also provide a reference for assessing the evolution of the performance of future RTTOV/MFASIS and IFS releases.

Overall, the best validation results are obtained for reflectances simulated in GOES-16 ABI channels 2 ( $0.64\mu\text{m}$ ) and 3 ( $0.86\mu\text{m}$ ). Reflectances simulated in channel 1 ( $0.47\mu\text{m}$ ) perform less well (see below). As expected, the statistical agreement between IRM and GOES turns out to be usually better in the extra-tropics than in the tropics, with smaller mean biases and much higher correlations, during both periods. Furthermore, the independent comparison of IFS with CERES TOA net broadband shortwave fluxes nicely supports the main conclusions about the origin of IFS+RTTOV/MFASIS–GOES reflectance biases.

The following main discrepancies between simulated IFS+RTTOV/MFASIS and GOES-16 ABI observed solar reflectances can be identified (in all three channels, unless otherwise stated):

- (1) Reflectances simulated in channel 1 ( $0.47\mu\text{m}$ ) suffer from a systematic "background" negative bias of around  $-6\%$  (in reflectance units) with respect to GOES observations. It is expected that the inclusion of multiple Rayleigh scattering in RTTOV version 13 will remove most of this particular bias. Further smaller improvement might also come from the use of actual cloud top height information from the model in MFASIS instead of a fixed value.
- (2) This study confirms that interpolation errors in MFASIS look-up table can lead to very large negative biases in reflectance near Earth's terminator, for solar zenith angles above  $80^\circ$ . Such special situations should therefore be discarded in all NWP applications, especially data assimilation.
- (3) Simulated reflectances in sunglint regions over sea are too high by about  $5\%$  (in reflectance units). Possible reasons for this include an underestimation of 10-metre wind speeds over oceans in the IFS or the computation of incorrect ocean wave spectra in RTTOV's sunglint parameterization.
- (4) In all three channels, high reflectances in thick cloud situations (e.g., deep convection; tropical cyclones) are systematically underestimated with IFS+RTTOV/MFASIS. This might point to some inadequacies in the specification of cloud liquid water and ice optical properties in RTTOV and/or to the need to add IFS convective hydrometeors as input to RTTOV/MFASIS (however, this information is not available from current operational forecasts). For cloud liquid water optical properties, the "Deff" option of RTTOV might be a better alternative than the OPAC option (see section 2.3.3), but this would require effective particle radii values to be explicitly provided by the user.
- (5) The IFS model predicts far too large cloud clusters in trade-wind regions over tropical oceans (especially over the South Pacific) during the local summer (resulting in a positive reflectance bias). Besides, the closed-cell nature of simulated clouds completely disagrees with the open-cell convec-

tion observed by GOES.

- (6) A strong negative reflectance mean bias (typ.  $-10$  to  $-30\%$ ), due to a systematic lack of low-level clouds (mainly stratocumuli) in the IFS, affects a large region along the north-eastern flank of the subtropical South Pacific Anticyclone (which moves closer to South America during the austral winter).
- (7) The IFS produces too much shallow convection over the Amazon region, especially during the dry season (NH summer).
- (8) The low-level clouds frequently seen on GOES visible images inside the eye of major tropical cyclones are missing in the IFS simulations. This might happen, for instance, if the model overestimates subsidence inside the eye.

Deficiencies in items (1), (2) and (3) are clearly linked to RTTOV/MFASIS and might therefore benefit from future upgrades of both RTTOV (version 13; [Saunders \*et al.\*, 2020](#); [Stumpf \*et al.\*, 2020](#)) and MFASIS (new neural-network-based version; [Scheck, 2021](#)). Issues in items (5), (6), (7) and (8) originate from the IFS and might be addressed through revisions of the relevant physical parametrizations. Assessing the impact of including aerosols on simulated reflectances would be interesting, but this would require either some substantial changes in RTTOV/MFASIS or the use of another offline simulator, such as FLOTSAM developed by Robin Hogan (ECMWF). Extending the validation to GOES-17 and MSG-SEVIRI (Spinning Enhanced Visible and InfraRed Imager) solar reflectances would help to further measure the performance of both IFS and RTTOV/MFASIS. In the case of MSG, it could also pave the way to the use of similar data from the coming MTG (Meteosat Third Generation) satellites, especially for data assimilation purposes. Finally, the validation of simulated solar reflectances could also be included in the evaluation of kilometre-scale experiments that will be run in the course of the DestinE and nextGEMS projects.

## Acknowledgements

The National Oceanic and Atmospheric Administration (NOAA, USA) should be acknowledged for granting access to the GOES-16 ABI Level-1b radiance data, via their Comprehensive Large Array-data Stewardship System (CLASS). Our thanks also go to the National Aeronautics and Space Administration (NASA, USA) for creating and distributing the CERES SYN1deg data. We are also very grateful to Robin Hogan (ECMWF) for his comments and suggestions during this work, to Alan Geer and Richard Forbes (ECMWF) for their careful review of the final draft, and to Leonhard Scheck (Ludwig Maximilian University, Munich) for his valuable advice on MFASIS.

## References

- Ahlgrimm, M., Forbes, R. M., Hogan, R. J. and Sandu, I. (2018). Understanding global model systematic shortwave radiation errors in subtropical marine boundary layer cloud regimes. *J. Adv. Model. Earth Syst.*, **10**(8), 2042–2060, doi:10.1029/2018MS001346.
- Bah, M., Gunshor, M. and Schmit, T. (2018). Generation of GOES-16 True Color Imagery without a Green Band. *Earth and Space Science*, **5**(9), 549–558, doi:10.1029/2018EA000379.
- Baum, B. A., Yang, P., Heymsfield, A. J., Schmitt, C. G., Xie, Y., Bansemer, A., Hu, Y.-X. and Zhang, Z.

- (2011). Improvements in Shortwave Bulk Scattering and Absorption Models for the Remote Sensing of Ice Clouds. *J. Appl. Meteor. Climatol.*, **50**(5), 1037–1056, doi:10.1175/2010JAMC2608.1.
- Betts, A. K. and Ball, J. H. (1997). Albedo over the boreal forest. *J. Geophys. Res.*, **1028**, 28901–28909, doi:10.1029/96JD03876.
- Courtier, P., Thépaut, J.-N. and Hollingsworth, A. (1994). A strategy for operational implementation of 4D-Var using an incremental approach. *Quart. J. Roy. Meteor. Soc.*, **120**, 1367–1388.
- Doelling, D. R., Loeb, N. G., Keyes, D. F., Nordeen, M. L., Morstad, D., Nguyen, C., Wielicki, B. A., Young, D. F. and Sun, M. (2013). Geostationary Enhanced Temporal Interpolation for CERES Flux Products. *J. Atmos. Oceanic Technol.*, **30**(6), 1072–1090, doi:10.1175/JTECH-D-12-00136.1.
- Elfouhaily, T., Chapron, B., Katsaros, K., and Vandemark, D. (1997). A unified directional spectrum for long and short wind-driven waves. *J. Geophys. Res.*, **102**(C7), 15781–15796, doi:10.1029/97JC00467.
- Escribano, J., Bozzo, A., Dubuisson, P., Flemming, J., Hogan, R. J., C.-Labonnote, L. and Boucher, O. (2019). A benchmark for testing the accuracy and computational cost of shortwave top-of-atmosphere reflectance calculations in clear-sky aerosol-laden atmospheres. *Geosci. Model Dev.*, **12**(2), 805–827, doi:10.5194/gmd-12-805-2019.
- Feingold, G., Koren, I., Wang, H., Xue, H. and Brewer, W. A. (2010). Precipitation-generated oscillations in open cellular cloud fields. *Nature*, **466**, 849–852, doi:10.1038/nature09314.
- Hess, M., Koepke, P. and Schult, I. (1998). Optical Properties of Aerosols and Clouds: The Software Package OPAC. *Bull. Amer. Meteor. Soc.*, **79**(5), 831–844, doi:10.1175/1520-0477(1998)079<0831:OPOAAC>2.0.CO;2.
- Kazumori, M., Geer, A. and English, S. J. (2016). Effects of all-sky assimilation of GCOM-W/AMSR2 radiances in the ECMWF numerical weather prediction system. *Quart. J. Roy. Meteor. Soc.*, **142**, 721–737, doi:10.1002/qj.2669.
- McFarquhar, G. M., Iacobellis, S. and Somerville, R. C. J. (2003). SCM Simulations of Tropical Ice Clouds Using Observationally Based Parameterizations of Microphysics. *J. Climate*, **16**(11), 1643–1664, doi:10.1175/1520-0442(2003)016<1643:SSOTIC>2.0.CO;2.
- Nuijens, L., Medeiros, B., Sandu, I. and Ahlgrimm, M. (2015). The behavior of trade-wind cloudiness in observations and models: The major cloud components and their variability. *J. Adv. Model. Earth Syst.*, **7**(2), 600–616, doi:10.1002/2014MS000390.
- Roesch, A., Gilgen, H., Wild, M. and Ohmura, A. (1999). Assessment of GCM simulated snow albedo using direct observations. *Climate Dyn.*, **15**, 405–418, doi:10.1007/s003820050290.
- Saunders, R., Hocking, J., Turner, E., Havemann, S., Geer, A., Lupu, C., Vidot, J., Chambon, P., C., K.-W., Scheck, L., Stiller, O., Stumpf, C. and Borbas, E. (2020). RTTOV-13 Science and Validation Report. *Technical report*, EUMETSAT, Report NWPSAF-MO-TV-046, available from EUMETSAT, 106 pages.
- Saunders, R., Hocking, J., Turner, E., Rayer, P., Rundle, D., Brunel, P., Vidot, J., Roquet, P., Matricardi, M., Geer, A., Bormann, N. and Lupu, C. (2018). An update on the RTTOV fast radiative transfer model (currently at version 12). *Geosci. Model Dev.*, **11**, 2717–2737, doi:10.5194/gmd-11-2717-2018.
- Scheck, L. (2021). A neural network based forward operator for visible satellite images and its adjoint. *J. Quant. Spectrosc. Radiat. Transf.*, **274**, 107841, doi:10.1016/j.jqsrt.2021.107841.

- Scheck, L., Frèrebeau, P., Buras-Schnell, R. and Mayer, B. (2016). A fast radiative transfer method for the simulation of visible satellite imagery. *J. Quant. Spectrosc. Radiat. Transf.*, **175**, 54–67, doi:10.1016/j.jqsrt.2016.02.008.
- Schmit, T. J., Griffith, P., Gunshor, M. M., Daniels, J. M., Goodman, S. J. and Lebar, W. J. (2017). A closer look at the ABI on GOES-R. *Bull. Amer. Meteor. Soc.*, **98**(4), 681–698, doi:10.1175/BAMS-D-15-00230.1.
- Schmit, T. J., Gunshor, M. M., Menzel, W. P., Gurka, J. J., Li, J. and Bachmeier, A. S. (2005). Introducing the next-generation advanced baseline imager on GOES-R. *Bull. Amer. Meteor. Soc.*, **86**(8), 1079–1096, doi:10.1175/BAMS-86-8-1079.
- Stamnes, K., Tsay, S.-C., Wiscombe, W. and Jayaweera, K. (1988). Numerically stable algorithm for discrete-ordinate-method radiative transfer in multiple scattering and emitting layered media. *Applied Optics*, **27**(12), 2502–2509, doi:10.1364/AO.27.002502.
- Stumpf, C., Scheck, L. and C., K.-W. (2020). MFASIS fit and interpolation errors in RTTOV v13 as a function of observation geometry. *Technical report*, EUMETSAT, NWP-SAF Note, available from EUMETSAT, 10 pages.
- Vidot, J. and Borbás, E. (2014). Land surface VIS/NIR BRDF atlas for RTTOV-11: model and validation against SEVIRI land SAF albedo product. *Quart. J. Roy. Meteor. Soc.*, **140**, 2186–2196, doi:10.1002/qj.2288.
- Yoshimori, K., Itoh, K. and Ichioka, Y. (1995). Optical characteristics of a wind-roughened water surface: a two dimensional theory. *Applied Optics*, **34**(27), 6236–6247.